Chapter 3 VISIBLE IMAGERY

We begin by looking in the part of the electromagnetic spectrum most familiar to humans - the visible spectrum. As an illustration, images from the first remote sensing satellite system are presented, from the CORONA spy satellites. Subsequent elements of the chapter look at elements of recognition (photo-interpretation), some basic optics, and the details of two high resolution imaging systems.

A The first remote sensing satellite - CORONA

1 A little history

CORONA was America's first operational space reconnaissance project. Its first successful mission was on August 18, 1960, and it operated for almost twelve years during the Cold War. It was developed as a highly classified program under the joint management of the CIA and the USAF, a relationship that evolved into the National Reconnaissance Office (NRO). For context, note that the first Soviet satellite, SPUTNIK, was launched on 14 October 1957. President Eisenhower endorsed the program in February 1958. This proved to be very foresighted, when Francis Gary Powers was shot down in a U-2 on 1 May 1960.

The first CORONA test launch was attempted 28 February 1959, followed by 12 failed missions. The Discover series (a cover name) had a dozen failures, 7 involving launch, 5 involving satellite/camera malfunctions. Mission number 13 produced the 1st successful recovery from space on 10 August 1960. The 1st image from space was taken on the next mission, on 18 August 1960. The last, #145, was launched 25 May 1972; the last images of the series were taken 31 May 1972.

Imaging resolution was originally 8 meters (25 feet), but improved to 2 meters (6 feet). Individual images on average covered an area approximately 10 miles by 120 miles. Operated for nearly 12 years, over 800,000 images were taken from space. The declassified collection includes 2.1 million feet of film in 39,000 cans.

2 The technology

The Corona vehicle was launched by a THOR booster and used the AGENA spacecraft as the upper stage. While in orbit, Corona took photographs with a constant rotating stereo panoramic camera system and loaded the exposed photographic film into recovery vehicles. The vehicles were de-orbited and recovered by Air Force C-119 aircraft while floating to earth on a parachute.

The cameras, designated with the codename Keyhole, began as variants on cameras designed for airphotos. The first cameras, the "C" series, were designed by Itek, and built by Fairchild. They used long film strips, 2.2" x 30", and an f/5.0 Tessar lens, with a focal length of 24". The first images hand a ground resolution of 40 feet, based on a film resolution of 50-100 lines/millimeter. (Advances in film technology by Kodak were some of the most important technology advances in the CORONA program.)

Improved camera, lens, and film design led to the KH4 series cameras, with Petzval, f3.5 lenses, still at 24" focal length. With film resolutions of 160 lines/mm, it was possible to resolve ground targets of six feet. (Negatives could be enlarged some 40 times.) CORONA ultimately used film ranging in speeds from ASA 2 to ASA 8 - 1% the speed of 'regular' film. This is the tradeoff for high film resolution, and is one reason the very large optics were needed. (Day et al, 1998, page 65). Infrared film was flown on Mission 1104 and used to photograph the Vandenberg AFB area. "Color film was flown on Mission 1105 and 1108…. By 1970, the CIA concluded that color film's decreased resolution made it relatively useless for intelligence purposes - black and white film had a resolution approximately twice as good as high resolution color film. But the color film could be useful for mineral resources exploration." (Day et al, 1998, page 82) The results indirectly led to the earth resources program, and hence, the Landsat satellites.

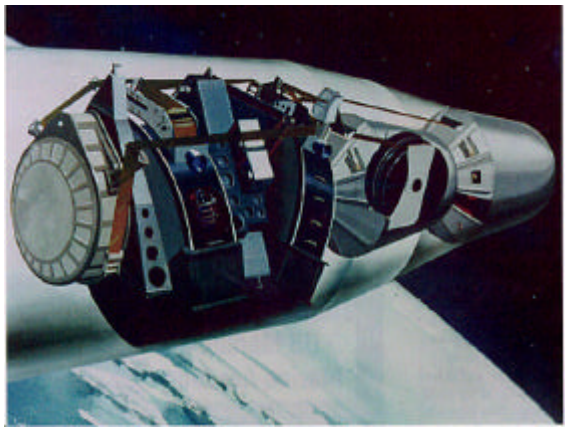

Figure 3-1 KH4B - artists concept

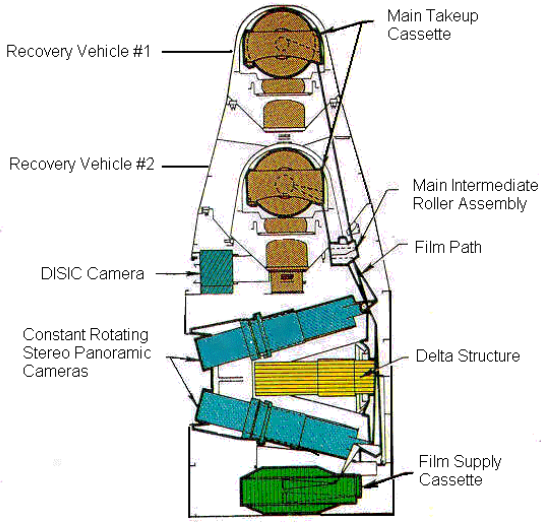

Figure 3-2 KH4B, or J3 camera. DISIC=Dual Improved Stellar Index Camera

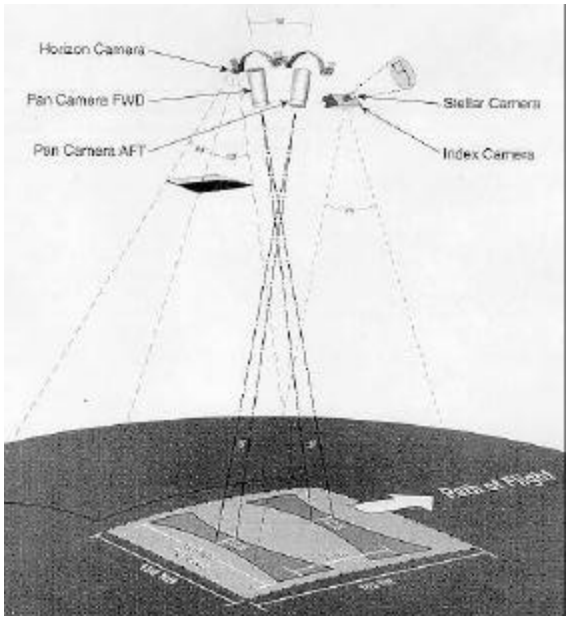

Figure 3-3. The KH4B cameras operated by mechanically scanning to keep the ground in focus. The paired cameras provided stereo images, which are very helpful for estimating the heights of cultural and natural features.

Figure 3-4. A U.S. Air Force C-119, and later, a C-130 (shown here) modified with poles, lines and winches extending from the rear cargo door captures a capsule ejected from a Discoverer satellite. Reportedly, this was considered by some to be the least likely part of the whole process - catching a satellite in midair.

3 Some illustrations

The first CORONA image, of the Mys Shmidta airfield, had high enough resolution to show the runway, and an adjacent parking apron.

Figure 3.5 Mys Shmidta Air Field, USSR. This August 18, 1960, photograph is the first intelligence target imaged from the first CORONA Mission. It shows a military airfield near Mys Schmidta on the Chukchi Sea in far-northeastern Russia.

Eventually, the systems got better, and higher resolution images were acquired

a) One always popular target - the Pentagon

b) Notice the shadow cast by the Washington monument.

Figure 3.6 Washington DC

Of course, the whole point was to spy on the Soviet Union. Here is Severodvinsk Shipyard, a North Sea port for the USSR, on 10 February 1969. The largish rectangular building in the center is the construction hall, and the square courtyard to the right is where vessels (submarines) are launched. The disturbed snow/ice (curved) trail is where they are floated into the river. The satellite is on a southbound pass over the port facility. (Eye in the Sky, The story of the Corona Spy Satellites, edited by Dwayne A Day, John M. Logsdon, and Brian Latell, 1998, page 224)

Figure 3.7 Severodvinsk Shipyard

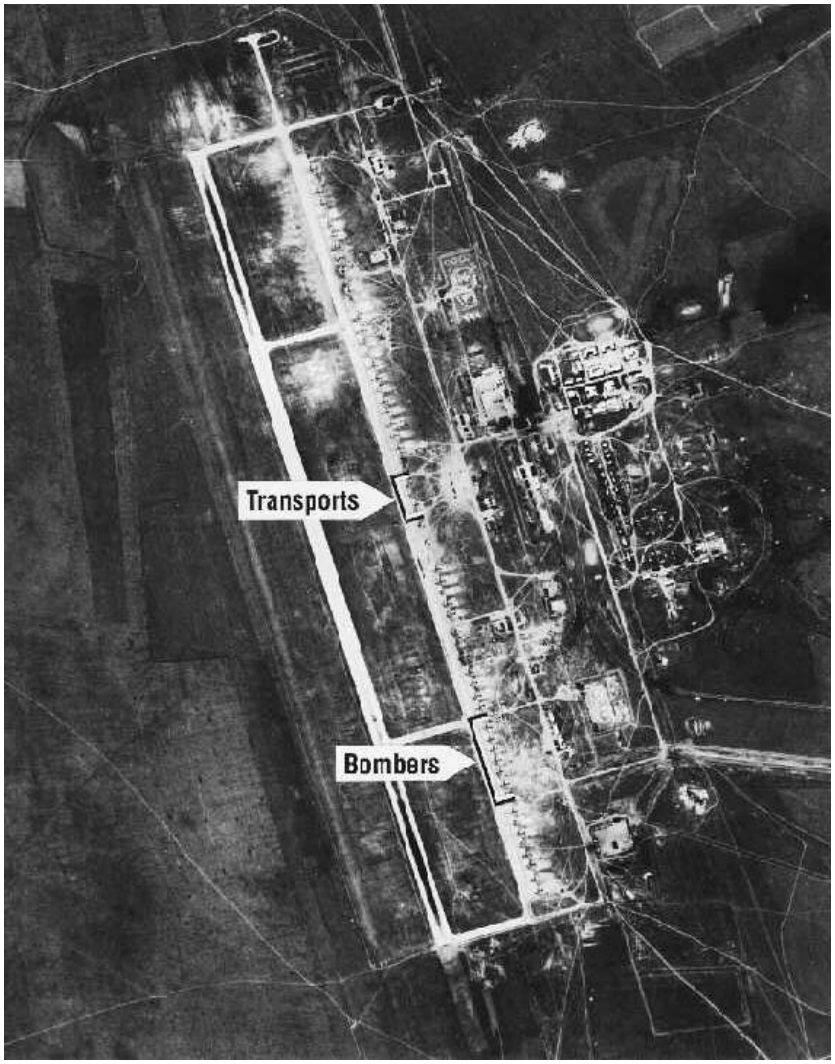

Figure 3.8
a) Air order of Battle is a fairly natural element of such imagery. The 5-10 foot resolution of the Keyhole camera systems was sufficient to distinguish classes of aircraft.

b) An image chip for the bombers indicated in the lower portion of the figure is displayed here.

B Interpretation keys (Elements of Recognition)

Having seen some of the early imagery, we now proceed to consider a few elements on the interpretation of imagery. The perspective used here is one developed for airphoto interpretation. (Avery and Berlin, pages 52-57)

1 Shape

One of the most useful elements of recognition is shape. One of the classic examples is the Pentagon, shown earlier in Figure 3-6. Note that in Figure 3-5, the airfield can be identified by the shape, even though it is not well resolved.

2 Size

Relative size is helpful in identifying objects; mensuration, the absolute measure of size, is extremely useful in extracting information from imagery. Illustrations at the beginning of Chapter 1 showed how runway length can be obtained from properly calibrated imagery. The Hen House radar sites (Figure 1-4) have characteristic shapes and sizes.

3 Pattern

Related to shape is pattern, the overall spatial form of related features. Figure 3-9 shows a Russian SAM site, with characteristic patterns that help detect the missile sites. A common illustration is the Russian propensity for putting three concentric fences around important installations.

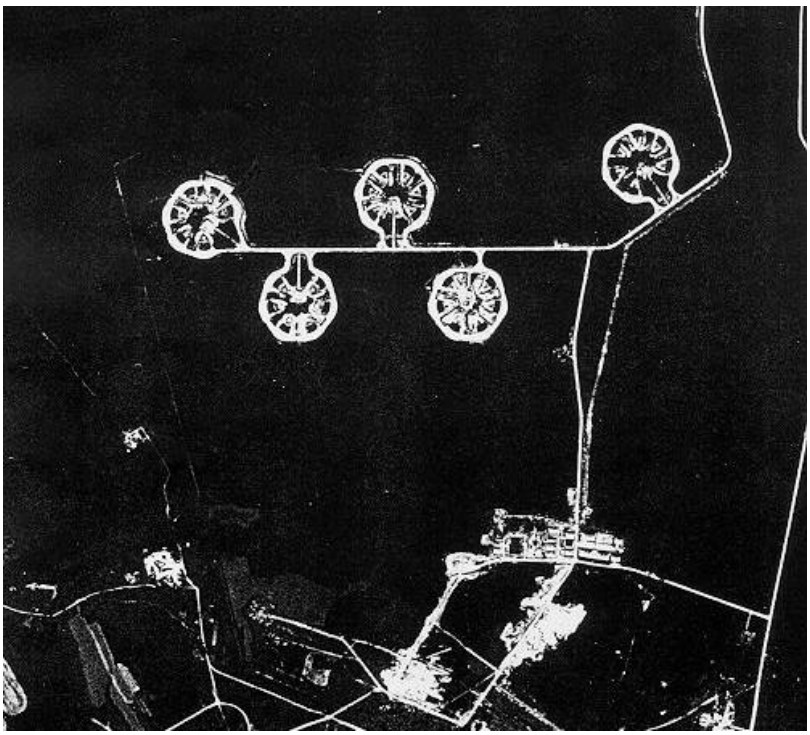

Figure 3.9 SA-2 SAM Base, KH-4 CORONA Product

4 Shadow

Shadows can be very helpful in separating targets from background. They can also be used to measure height. See the Washington monument illustration (Figure 3-6b).

5 Tone or color

Tone and color are the product of the target albedo, and illumination. The Landsat images in chapter 1 are good illustrations of this element. Consider the difference in tone between the runway (asphalt?) and adjacent regions in Figure 1-10b. The green regions on the south end of Coronado island can be distinguished from regions of similar brightness by the color. On a larger scale, the distinction between dirt and vegetation in San Diego County can also be made in color.

6 Texture

Texture depends upon the image scale, but can be used to distinguish objects which may not otherwise be resolved. The relative coarseness or smoothness of a surface becomes a particularly important visual clue with radar data. (Figure 1-19 b)

7 Association

"Certain objects are genetically linked to other objects, so that identifying one tends to indicate or confirm the other. Association is one of the most helpful clues for identifying cultural features." Avery and Berlin (1992). Things like nuclear power plants, for example, tend to be near source of cooling water, though this can also be associated with our last characteristic, which is site or location.

8 Site

This element is the location of an object relative to its environment.

C Some very simple geometric optics

1 Focal Length/Geometry

The most fundamental equation in optics is the thin lens equation:

$$\frac{1}{f} = \frac{1}{i} + \frac{1}{o} \qquad \text{(Eqn. 3-1)}$$

Here, f is the 'focal length', and intrinsic characteristic of the lens determined by the radius of curvature and the index of refraction of the lens material(s). The distances from the center of the lens to the object (o) and to the image (i) then are the other two parameters. We see that the focal length defines the image distance when o, the object distance, is infinity (∞). In the illustration here, the object distance is twice the focal length, so the image distance is also twice the focal length (I=O=2f).

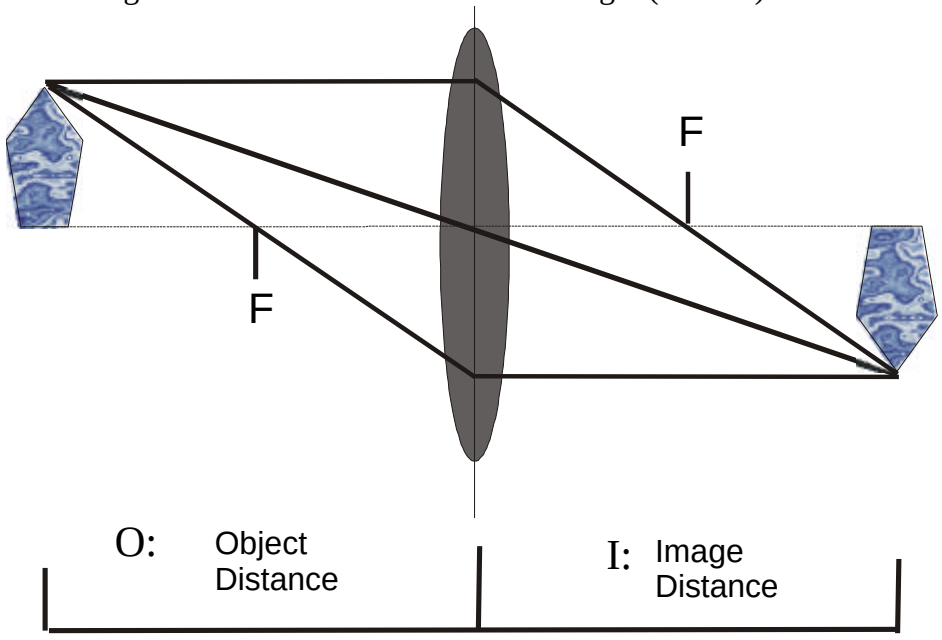

Figure 3.10 Thin lens law

2 Optical Diagram - Similar Triangles - Magnification

The size of the image is determined by the old geometry law of similar triangles - the magnification is equal to the ratio of the object distance to the image distance. In the example above, the two are equal so the image has the same size as the object. Normally, in remote sensing, the object distance is a large number, while the image distance is roughly the focal length. For example, the handheld camera on the shuttle is typically used with a 250 mm lens, at an altitude of 150 km. So, the ratio of the image size to the object is $\frac{250\times10^{-3}}{150\times10^{3}} = 1.6\times10^{-6}$ - a pretty small number. The Monterey Peninsula

(extending some 20 km from north to south) would be imaged on a piece of film 0.032 m in length (32 mm - roughly the width of normal 35 mm film).

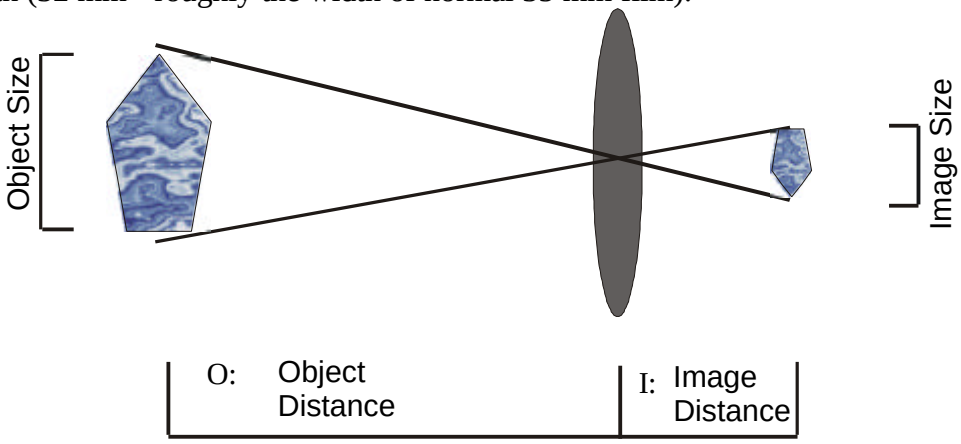

Figure 3.11 Magnification - similar triangles

3 Aperture (F/stop)

The light gathering ability of a lens is defined by the diameter of the lens - the bigger the better in optics! Still, the effectiveness of a given aperture depends upon the focal length (magnification). This dependence is defined by the concept of the f number, or f/stop. It is defined as the ratio of the focal length to the lens (or mirror) diameter.

$$f/\# = \frac{\text{Focal Length}}{\text{Diameter of the Primary Optic}} \qquad \text{(Eqn. 3-2)}$$

Typical camera lenses found on amateur cameras will vary from f/2.8 to f/4. High quality 'standard' lenses will be f/1.2 to f/1.4 for 35mm cameras. The longer the focal length (higher magnification), the large the lens needs to be. A typical telephoto for a sports photographer might be 500 mm, and might at best be f/8. (What is the diameter implied by that aperture?)

D Diffraction Limits

Light propagates as a wave, and hence does not propagate exclusively in straight lines. In common experience, this is more commonly encountered in situations where sound waves bend around barriers. A short theoretical development of the concept is given here. The foundation concept of interference is developed using the classic Young's Double Slit experiment.

Young's Double Slit experiment is based on the wave theory of light, and the understanding that waves can interfere with one another. In the drawing below, light can pass through either of the two small apertures shown, and travel to the right, hitting the screen at x, which is some distance in the vertical direction from the center line. The two

light rays will travel different distances, R_1 and R_2. Because of this difference, the two sets of waves will be somewhat out of phase. The difference in phase is just:

$$\Delta\Phi = 2p\frac{R_2 - R_1}{l} \qquad \text{(Eqn. 3-3)}$$

We want to relate this difference in phase to the distances R and x. Note that for satellites, R is the altitude, x will be the distance between two targets on the ground.

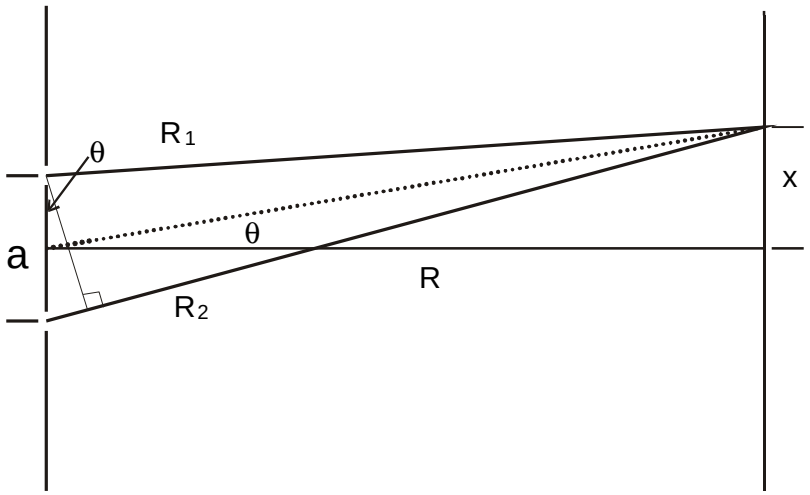

Figure 3.12 Young's Double Slit Experiment

Because the distance R is large compared to x or a, we can approximate:

$$q \approx \sin q \approx \tan q \approx \frac{x}{R} \qquad \text{(Eqn. 3-4)}$$

The two triangles shown are similar, and so we get the ratios:

$$\frac{R_2 - R_1}{a} = \frac{x}{R} \qquad \text{(Eqn. 3-5)}$$

From this, we can get the difference in phase between the light from the two slits:

$$\Delta\Phi = 2p\frac{R_2 - R_1}{l} = 2p\frac{a\,x}{l\,R} = 2p\frac{a}{l}\sin q \qquad \text{(Eqn. 3.6)}$$

If the phase difference is π, the waves will cancel, and there will be a dark spot on the screen. The next bright spot will appear when the phase difference is 2π, followed by a minimum at 3π, and so on. If the intensity is plotted, a pattern like this occurs:

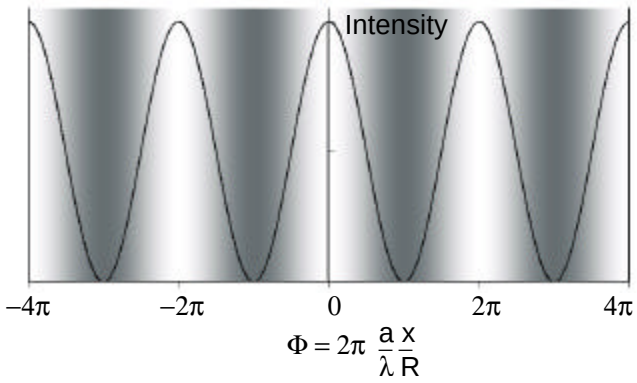

Figure 3.13 Double slit diffraction pattern. *Intensity* $\propto \text{sinc}^2\Phi$

The distance between two peaks is 2π, so the separations will be such that

$$\Delta\Phi = 2\pi = 2\pi\frac{a\,x}{\lambda\,R} = 2\pi\frac{a}{\lambda}\sin\theta;\ \text{ or } \frac{a\,x}{\lambda\,R} = 1 \quad \Rightarrow \quad \Delta x = \frac{l\,R}{a} \qquad \text{(Eqn. 3.7)}$$

What does this have to do with optical instruments? The real answer lies in a fair amount more work, unfortunately. The extrapolation of this idea to optical systems is fairly simple, however. The above illustration considers light from two small sources (slits). Conceptually, however, these could be two of the many small points on the surface of a lens. Light passing through different parts of the lens can interact with itself, causing interference. The smaller the lens (the smaller a is, above), the larger this effect will be. The quantity Δx above becomes the separation between two points on the ground, or two stars in the sky that can be resolved. Once the mathematics is completed, a formula for the intensity of light passing through a circular aperture can be obtained that uses Bessel functions:

$$I \propto \left[\frac{J_1(w)}{w}\right]^2, \text{ where } w = \frac{2\pi\,a\,r}{R\,\lambda}. \qquad \text{(Eqn. 3.8)}$$

J_1=the 'J' Bessel function of order 1.
a = lens radius,
r = distance from center line,
R = distance from lens to screen, and
λ = wavelength.

This function looks like this:

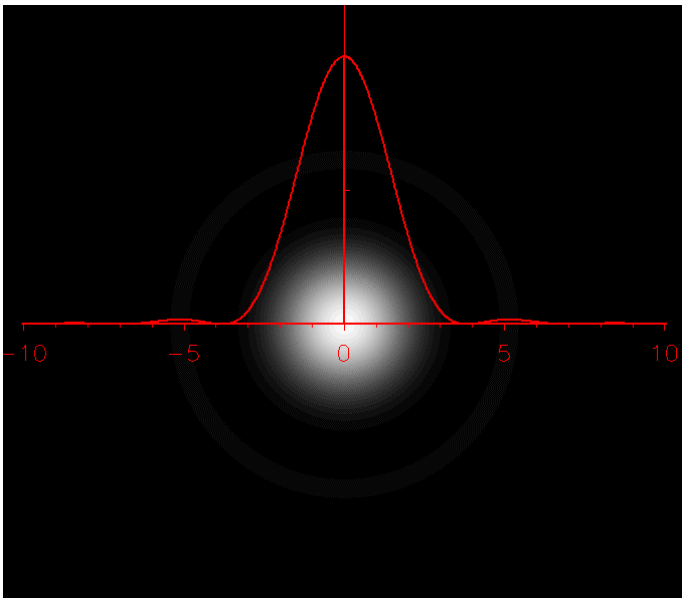

Figure 3.14

The first zero occurs where $w = 3.832$, which leads to a relatively famous result, that the radius of the 'Airy Disk' = 0.61*λ*distance/lens radius, or that the angular resolution of a lens is:

$$\Delta\theta = 0.61 \bullet \frac{\lambda}{a}, \text{ or } \Delta\theta = 1.22 \bullet \frac{\lambda}{\text{diameter}} \qquad \text{(Eqn. 3.9)}$$

For most purposes in these notes, we ignore the factor of 1.22.

Application:
Hubble like system orbiting at 200 nautical miles = 370 km
Mirror diameter = 96 inches = 2.43 meters (acts like lens diameter)
wavelength = 5000 Angstroms = 5×10^{-7} m

Ground Separation Distance (GSD) =

$$\Delta x = \frac{l\ R}{a} = \frac{5\times10^{-7} \bullet 370\times10^{3}}{2.43} = 7.5\times10^{-2} \text{ m} = 7.5 \text{ cm or } 3''$$

E Atmospheric Absorption, scattering, and turbulence

There are three limiting factors which the atmosphere introduces into remote sensing. These are absorption, typically by atomic and molecular processes; scattering, which is primarily due to aerosols (dust, fog, smoke); and turbulence, which is due to fluctuations in the temperature and density of the atmosphere. The first two terms combine to produce the effects illustrated in Figure 3.15, which shows a standard model for atmospheric absorption.

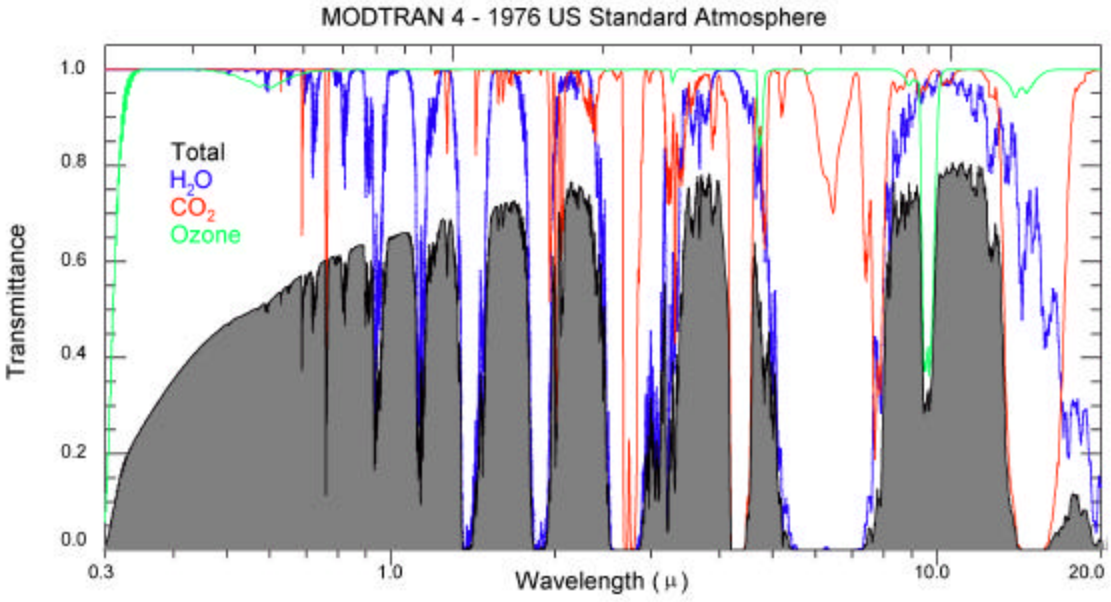

Figure 3.15 Atmospheric absorptions. Transmission curve calculated using MODTRAN 4.0, release 2. The total transmission is plotted, along with the effects for some of the primary atmospheric absorption elements - water, carbon dioxide, and ozone. Conditions are typical of mid-latitudes, with the 1976 US standard atmosphere assumed. The overall broad shape is due to scattering by molecular species and aerosols.

1 Atmospheric Scattering

Electromagnetic radiation within certain sections of the ultraviolet, visible, and reflected infrared bands is impeded in its direct journey through the atmosphere by the scattering process, which disperses the radiation in all directions. Important scattering agents include gaseous molecules, suspended particulates called aerosols, and clouds. Three types of atmospheric scattering are important to remote sensing.

Rayleigh, or **molecular, scattering** is primarily caused by oxygen and nitrogen molecules whose effective diameters are at least 0.1 times smaller than the affected wavelengths. Rayleigh scattering is most influential at altitudes above 4.5 km, occurring in what is called the **pure atmosphere.** The amount of Rayleigh scattering is highly selective, being inversely proportional to the fourth power of wavelength (λ^{-4}) (Figure 3-16). Consequently, invisible ultraviolet radiation, at a wavelength of 0.3 μ, is scattered 16

times as readily as red wavelengths at 0.6 μ [$(0.6/0.3)^4$]. In the visible spectrum, blue wavelengths at 0.4 μ are scattered about five times as readily as red wavelengths at 0.6 μ [$(0.6/0.4)^4$]. The preferential scattered of blue wavelengths explains why the clear sky (i.e., low humidity and few aerosols) appears blue in daylight. The blue wavelengths reach our eyes from all parts of the sky.

Mie, or **nonmolecular, scattering** occurs when there are sufficient particles in the atmosphere that have mean diameters from about 0.1 to 10 times larger than the wavelengths under consideration. Important Mie scattering agents include water vapor and tiny particles of smoke, dust, volcanic ejecta, and salt crystals released from the evaporation of sea spray. The influence of Mie scattering is most pronounced in the lower 4.5 km of the atmosphere, where the larger Mie particles are most abundant (i.e., in the impure atmosphere). Mie scattering influences longer radiation wavelengths than Rayleigh scattering. Depending upon the size distribution and concentration of Mie particles, the wavelength dependence varies between λ^{-4} and λ^{0}.

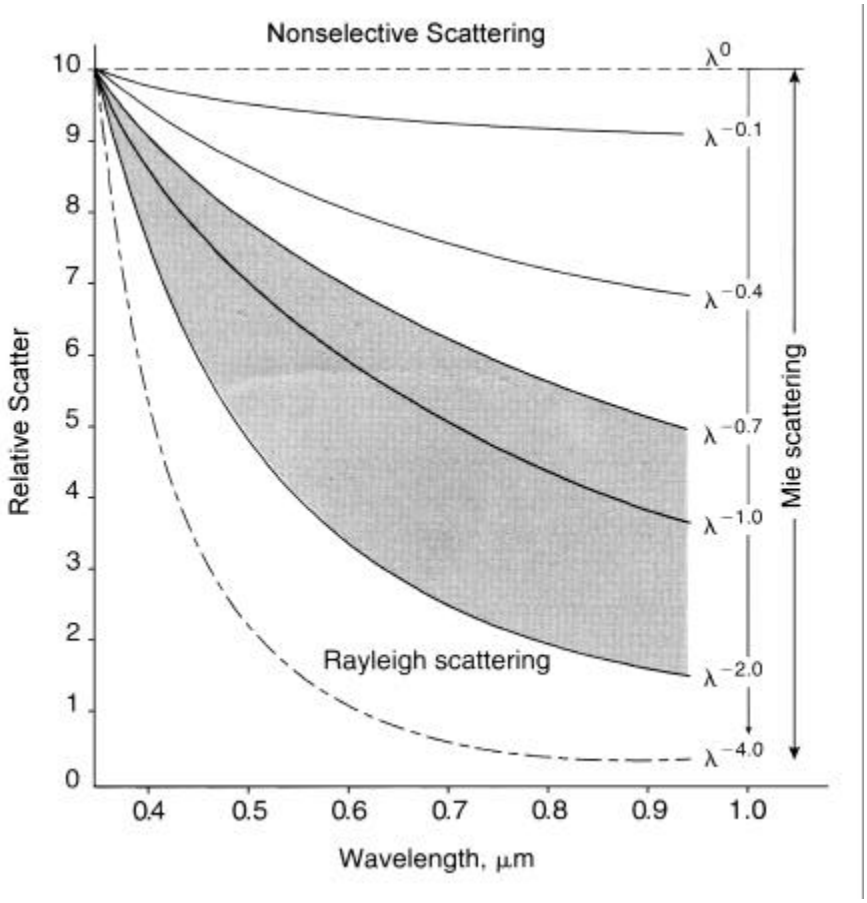

Figure 3.16 Atmospheric Scattering

The clear atmosphere is a medium for both Rayleigh and Mie scattering. For a range of typical atmospheres, their combined influence is from about $\lambda^{-0.7}$ to λ^{-2} (Figure 3-16). Using a λ^{-2} relationship, blue wavelengths at 0.4 μ are scattered about three times as readily as red wavelengths at 0.7 μ [$(0.7/0.4)^{-4}$]. The observation of a red sunrise or

sunset is caused by the preferential treatment of Rayleigh and Mie scattering agents on sunlight. At these times, the solar beam, which starts out as white light, passes through its longest atmospheric path. This extended path causes the shorter wavelengths of sunlight to be scattered away (blue and green), leaving only the red wavelengths to reach our eyes.

Nonselective scattering becomes operative when the lower atmosphere contains a sufficient number of suspended aerosols having diameters at least 10 times larger than the wavelengths under consideration. Important agents include the larger equivalents of Mie particles plus the water droplets and ice crystals of which clouds and fog are composed. Non-selective scattering is independent of wavelength (λ^0). Its influence spans the near ultraviolet and visible bands and extends into the reflected infrared band (Figure 3-16).

Within the visible band, colorless water droplets and ice crystals scatter all wavelengths equally well, causing, for example, the sunlit surfaces of clouds to appear brilliant white. Also, large smog particles, if not possessing special absorption properties, will cause the color of the sky to go from blue to grayish white.

2 Atmospheric Turbulence

The third limiting factor in remote sensing through the atmosphere is atmospheric turbulence, which might also be termed the question: Why do stars twinkle? The answer is illustrated by Figure 3.17. This effect is much greater looking up out through the atmosphere than looking down at the earth.

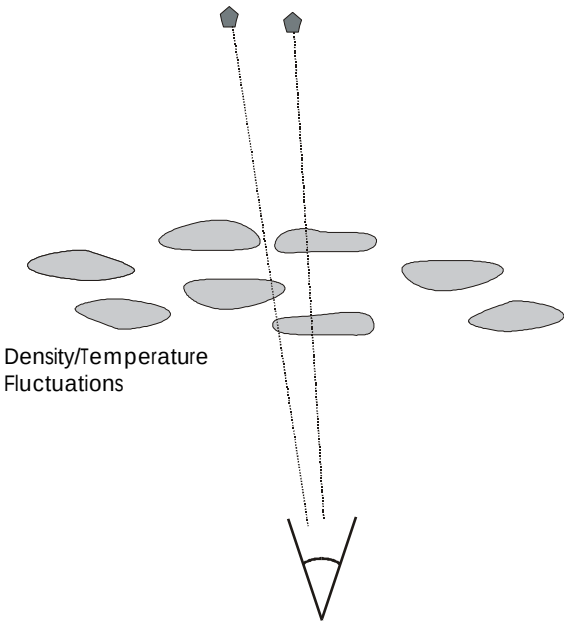

Figure 3.17 a
Light propagating down through the atmosphere will encounter small perturbations of density and temperature, due to turbulent processes in the atmosphere. These small fluctuations produce variations in the index of refraction, which in turn cause small fluctuations in the direction in which the light is propagating.

Figure 3.17 b, c
First light for the adaptive optics system on the 3.5-m telescope at the Starfire Optical Range occurred in September, 1997. This astronomical I Band (850 nm) compensated image of the binary star Kappa-Pegasus (k-peg) was generated using the 756 active actuator adaptive optics system. The two stars are seperated by 1.4544 microradians (4.85 microradians/arcsecond). The images are 128x128 pixels - each pixel subtends 120 nano-radians, or 3.17 arcsec. The FWHM of the uncompensated spot is about 7.5 microradians - about 5 times the separation of the two stars.

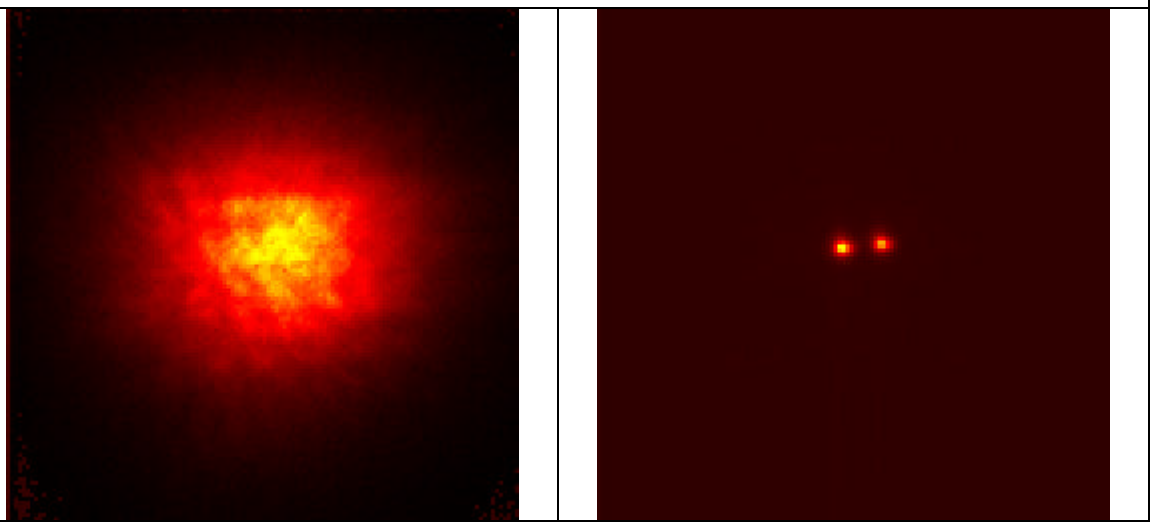

Note on nomenclature:
Astronomy IR Bands are: H (1.65 microns), I (0.834 microns),J (1.25 microns), K (2.2 microns).

Summary: there are three factors which constrain the resolution which can be obtained with an imaging system: diffraction (the Rayleigh criterion), scattering, and turbulence.

F Detectors

The other primary element in any sensor system is the detector behind the optics. Historically, there have been two primary techniques: film and solid state.

1 Film

The role of film in remote sensing is an increasingly historical one, as the last of the space-based film systems (notably the Russian SPIN system) are being phased out. There is still a substantial airborne film imaging community, but this is also evaporating fairly rapidly, at least on the military side.

2 Solid State

Generally speaking, the detectors involved in remote sensing utilize arrays of solid-state detectors, much like the CCD detectors in modern video cameras, and digital still cameras. Though not a bad starting point, this rather broad statement about the class of sensors also termed focal plane arrays (FPA's), does not properly take into account the many sensors today flying linear arrays (1-dimensional focal planes) as on SPOT, and even the ongoing use of single detector sensors, such as on GOES and Landsat. Still, the underlying physics is similar for most such sensors.

Just as with the Bohr atom, as developed in Chapter 2, solid materials, and in particular semi-conductors, have a distribution of energy levels which may be occupied by electrons. Generally, the electrons reside in a state corresponding to the ground state of an individual atom, termed the Valence Band. There is then a gap in energy (a "bandgap"), which represents a range of energies that are forbidden for the electron to occupy.

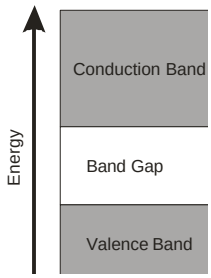

Figure 3.18

If a photon hits the semiconductor, however, it can give energy to an electron in the valence band, exciting it up into the conduction band. The significance of this is that it is now possible for the electron to move as though in a conductor, and it can be collected and measured. This is the essence of the detection mechanism for most solid state detectors. Such detectors have an efficiency that varies, but typically 40-80% of the incident photons with sufficient energy can be detected.

Material	Bandgap energy (eV) at 300 K
Silicon	1.12
Germanium	0.66
Gallium Arsenide	1.424
Indium Antimonide	?
Platinum Silicide	?
HgCdTe	0.1 to 0.3

This simple description makes it possible to quickly follow some of the more important constraints in the use of solid state detectors. First, one must match the energy bandgap to the energy of the photons you wish to observe. The photon energy must be at least

equal to the size of the bandgap, which varies with material. (Find the values for Platinum Silicide (PtSi), and Indium Antimonide (InSb))

What limits do these values place on the utility of different materials for use as detectors? Taking silicon as the most common example, we recall from Chapter 2 the equation which relates wavelength to the energy in a transition:

$$\lambda = \frac{hc}{\Delta E}$$

Here, ΔE is the band gap energy (in eV), and we use:

$$\lambda = \frac{hc}{\Delta E} = \frac{1.24\times10^{-6}\ (\text{eV m})}{1.12\ \text{eV}} = 1.1\times10^{-6}\ \text{m}, \text{ or } 1.1 \text{ microns.}$$

So, the visible and the first part of the near-infrared spectrum can be detected with silicon detectors. This is reflected in their common usage in modern cameras.

The detection of longer wavelength photons requires the usage of materials such as HgCdTe, or InSb. The relatively small bandgaps cause a problem, however. At room temperature, the electrons tend to rattle around a fair amount, and every now and then one will cross the gap, just based on thermal excitation. This is a process which is largely controlled by the exponential term which comes from the "Maxwell-Boltzmann" distribution (bell-shaped curve) which describes the velocities, or energies, which will be found in any collection of objects (electrons, atoms, molecules) in a thermal equilibrium:

$$number \propto e^{-\frac{\text{Bandgap Energy}}{\text{Thermal Energy (kT)}}} \qquad \text{(Eqn. 3-10)}$$

If collected, this becomes part of a background noise termed the "dark current". In order to prevent this, the materials must be cooled - typically to 50-70 K, which requires liquid nitrogen cooling at least, and for some applications, liquid helium (4 K). Mechanical refrigerators can also be used, but are a concern in space applications.

Quick illustration of why cooling is important:

Use HgCdTe, assume a Bandgap of 0.1 eV, and compare the nominal number of electrons above the band gap at room temperature (300 K) and at 4 K. Note that the conversion factor "k" in the term "kT" is:

$$1.38\times10^{-23}\ \frac{\text{Joules}}{\text{Kelvin}} \Big/ 1.6\times10^{-19}\ \frac{\text{Joules}}{\text{eV}} = 8.62\times10^{-5}\ \frac{\text{eV}}{\text{Kelvin}}$$

T = 300 K: $kT = 0.026$ eV ; T = 4 K , $kT = 0.00035$ eV

$$number \propto e^{-\frac{\text{Bandgap Energy}}{\text{Thermal Energy (kT)}}} = \begin{cases} e^{-\frac{0.1}{0.026}} = e^{-3.8} = 0.02 \ @300\text{ K} \\ e^{-\frac{0.1}{0.00035}} = e^{-286} \approx 0 \quad @ \quad 4\text{ K} \end{cases}$$

At room temperature, the exponential is small, but reflects a non-negligible number of excitations of electron above the band gap energy. In liquid helium, the electrons sit quietly below the band gap.

Visible imaging cameras uniformly use silicon as the sensitive element. As of this writing, one finds that typical commercial infrared imaging systems that use InSb, PtSi, and HgCdTe. (e.g. FLIR systems family of cameras). In addition, there are two popular new technologies: quantum well (QWIP) and micro-bolometer detectors. The latter in particular offers a variety of advantages over the more traditional cooled semi-conductor systems.

3 Focal Plane Arrays

The photo-sensitive component of a detector can exist as a single element, and there are a number of operational systems which nominally have a single detector. A notable current example would be the GOES weather satellite, described in a subsequent chapter. Generally, however, newer systems are comprised of either linear arrays of pixels, as will be seen below for IKONOS, with an array which is 1x13,500 pixels, or by rectangular arrays. The latter currently would be something like the 640x480 CCD arrays found in a low-cost electronic camera.

A CCD (charge coupled device) is an array of sensitive elements,

The CCD imager evolved from a low-cost memory element in 1970, called a charge-coupled device (CCD). The CCD is an integrated circuit (IC) with the unique property that a charge held in one cell of the IC can be shifted to an adjacent cell by applying a suitable shift pulse. Information defined by the amount of charge can be shifted from cell to cell with virtually no loss. When it was further discovered that the construction could be altered so that individual cells also responded to incident light while retaining the ability to shift charges, the dream of a solid-state imager was born.

Many charge coupled cells or picture elements are arranged in a rectangular array. Each picture element, also called a pixel of the array, converts incoming light into a charge directly proportional to the amount of light received. This charge is then clocked (shifted) from cell to cell, to be finally converted to a video signal that represents the original image, at the output of the CCD.

4 Uncooled Focal Planes - Microbolometers

One of the problems with the traditional technology associated with semi-conductor detectors is the need for cooling. This is because cooling either requires a coolant (e.g. liquid nitrogen), or a mechanical refrigeration technique. The former is often awkward in the field, and for space use a finite supply of coolant defines a limit on detector lifetime. Mechanical devices are in general problematic for space use, because of a concern over mechanical failure.

Microbolometer techniques approach the detection process by sensing the change in temperature of a sensitive element, typically by measuring the resistance of that element. This allows the direct detection of "heat", as opposed to counting photons directly. As a consequence, the detectors do not need to be cooled. Commercial IR cameras are now being manufactured using these detectors, and they are very popular for applications such as fire-fighting. Such cameras at present are not quite as sensitive, and do not presently have the resolution of the more traditional technologies.

G Imaging system types

Remote sensing systems can generally be divided in to a handful of basic types, depending upon the form of imaging technology being used. These distinctions will affect the resolution and sensitivity of the system, and to a certain extent, the quality of the data.

1 Framing systems - mostly film systems (Corona)

Framing systems are those that snap an image, much like a common film camera, or a modern digital (still or video) camera. An image is formed on a focal plane, and the image is stored via chemical (film) or electronic (CCD) means. Variants on this technique are used by some air-photo systems, and the early Corona satellites, where the film is moved in concert with the satellite motion, to maintain a longer exposure time and better focus.

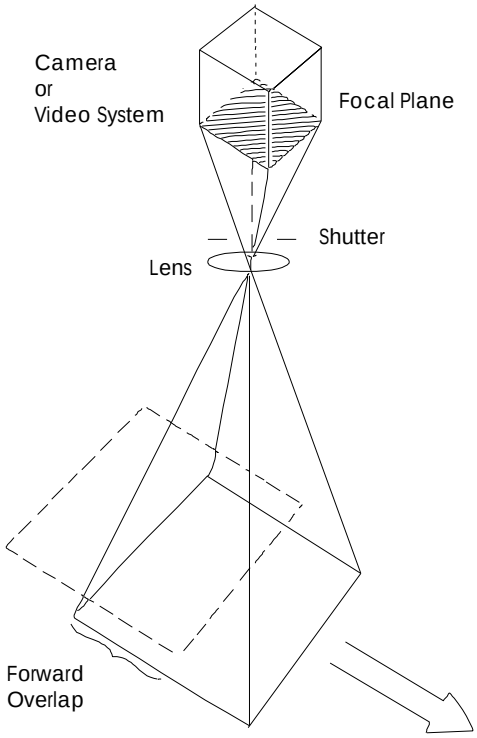

Figure 3-19. Framing System

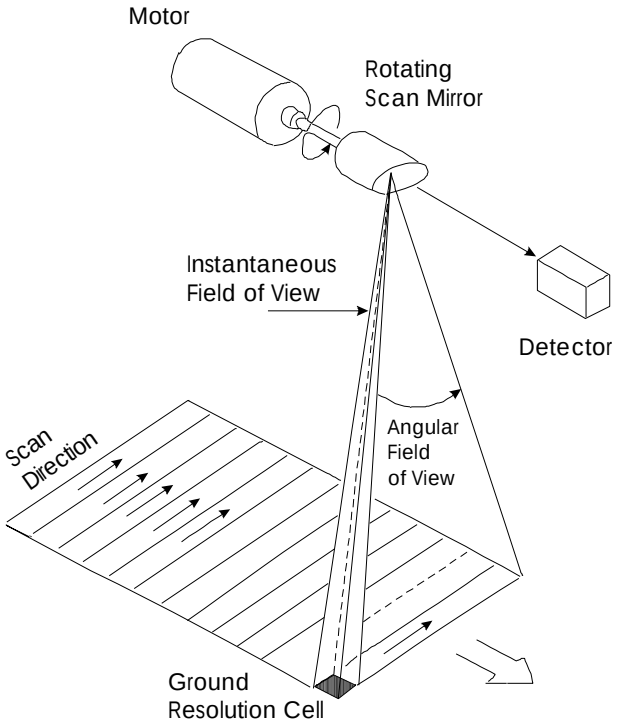

Figure 3-20. Cross-Track Scanner

2 Scanning Systems

a Cross Track (Landsat MSS, TM; AVIRIS)

Sensors such as those on the GOES weather satellite and the Landsat system consist of a small number of detectors - from one to 32 or so in the systems described later in the text. The sensor is swept from side to side, typically via an oscillating mirror, while the system flies along-track. The image is built up by the combined motion of the optic and the platform (aircraft or satellite).

b Along Track (SPOT HRV)

Linear detector arrays are used in systems such as the SPOT HRV sensor. The 'cross-track' dimension is covered by the linear array, while the along track direction is covered by the motion of the satellite.

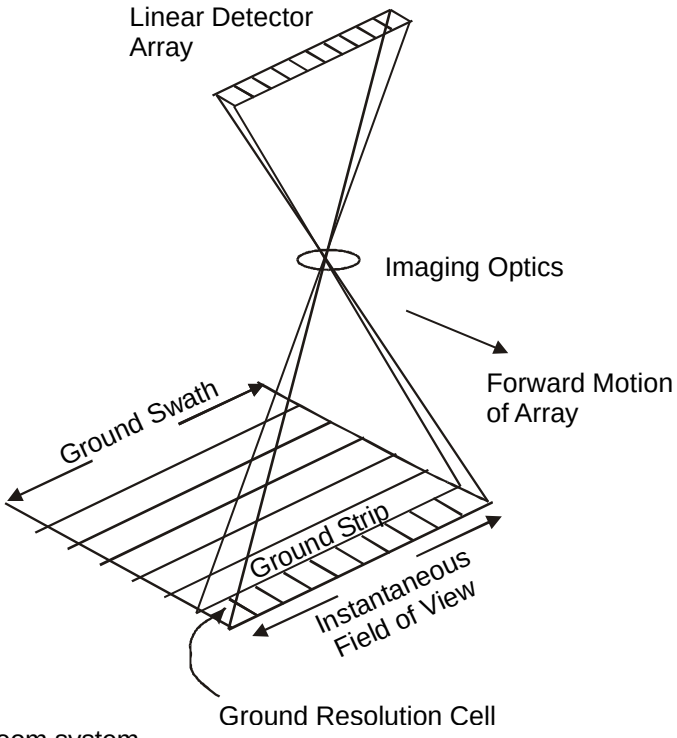

Figure 3.21 Pushbroom system

In subsequent sections we will consider how these techniques have been implemented in space imaging systems.

H Hubble - The Space Telescope

Three modern systems are described below, beginning with a fairly detailed consideration of the Hubble Space Telescope. Following that, the commercial IKONOS satellite will be briefly described, and a brief presentation of the low-light level imaging capability of DMPS will be made.

1 The Hubble Satellite

The Hubble Space Telescope (HST) was deployed April 25, 1990 from the space shuttle Discovery (STS-31). It has since been serviced three times, on the STS-61 shuttle mission launched on December 2, 1993, and then again on STS-82, launched on February 11, 1997, and on STS-103 launched on December 19, 1999.

Figure 3.22 The initial deployment of the Hubble Space Telescope.

STS 61 was the fifth flight of the Endeavour orbiter. Its objective was to repair, replace, and update the instruments on the Hubble Space Telescope. During several days of EVA, the crew installed corrective optics (COSTAR) in the light path after removing the High Speed Photometer (HSP) instrument; replaced the older Wide Field/Planetary Camera (WF/PC) with a newer version (WFPC 2); and replaced malfunctioning solar arrays.

The STS-82 mission had similar goals. During several days of EVA, the crew replaced a failed Fine Guidance Sensor (FGS), swapped one of the reel-to-reel tape recorders with a solid-state recorder, and exchanged two of the original instruments, the Goddard High-Resolution Spectrograph (GHRS) and the Faint Object Spectrograph (FOS), with two new instruments, the Space Telescope Imaging Spectrograph (STIS) and the Near Infrared Camera and Multi-Object Spectrometer (NICMOS). In addition to this planned work, astronauts discovered that some of the insulation around the light shield portion of

the telescope had degraded and attached several thermal insulation blankets to correct the problem.

The STS-103 mission was launched to replace the 6 gyroscopes, after the failure of 4 of the old gyros. In addition to the gyros, astronauts also replaced a guidance sensor and a transmitter, installed a new, advanced central computer, a digital data recorder, battery improvement kits, and new outer layers of thermal protection.

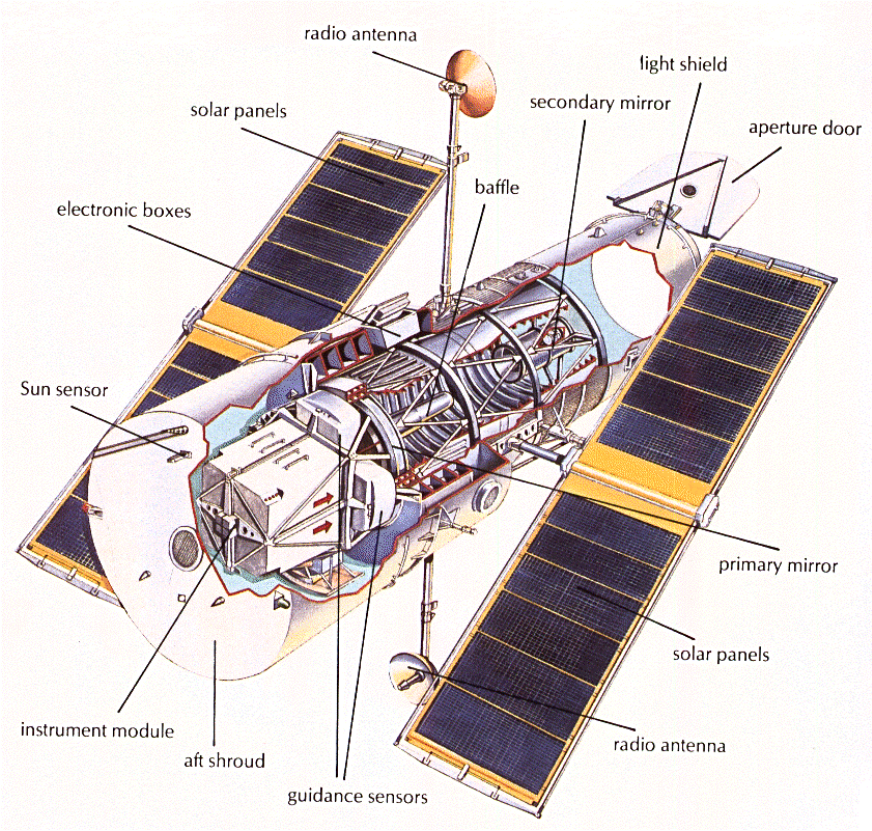

Figure 3.23 The Hubble satellite.

HST is roughly cylindrical in shape, 13.1 m end-to-end and 4.3 m in diameter at its widest point. The ten-ton vehicle is three-axis-stabilized. Maneuvering is performed via four of six gyros, or reaction wheels. Pointing can be maintained in this mode (coarse track) or the Fine Guidance Sensors (FGSs) can be used to lock onto guide stars (fine lock) to reduce the spacecraft drift and increase the pointing accuracy. It has a pointing accuracy of 0.007 arc-seconds.

Power to the two on-board computers and the scientific instruments is provided by two 2.4 x 12.1 m solar panels, which provide a nominal total power of 5 kW. The power generated by the arrays is used to power the satellite system (about 1.3 kW), and the science instruments (1-1.5 kW), and charge the six nickel-hydrogen batteries needed to provide power to the spacecraft during the roughly 25 minutes per orbit in which HST is within the Earth's shadow. (ref: e-mail from Dr. J. Keith Kalinowski, NASA/GSFC, 3 August, 1999)

Communications with the satellite are maintained with the TDRSS satellites. Observations taken during the time when neither TDRSS is visible from the spacecraft are recorded and dumped during periods of visibility. The spacecraft also supports real-time interactions with the ground system during times of TDRSS visibility. The primary data-link is at 1024 kbps.

There are two interesting constraints on the satellite behavior which are instructive, and which will affect most any LEO satellite.

South Atlantic Anomaly
Above South America and the South Atlantic Ocean lies a lower extension of the Van Allen radiation belts called the South Atlantic Anomaly (SAA). No astronomical or calibration observations are possible during passages of the spacecraft through the SAA because of the high background induced in the detectors. SAA passages limit the longest possible uninterrupted exposures, to about 12 hours (or 8 orbits).

Spacecraft Position in Orbit
Because HST's orbit is low, atmospheric drag is significant. Moreover, the amount of drag varies, depending on the orientation of the telescope and the density of the atmosphere, which depends on the level of solar activity. The chief manifestation of this effect is that it is difficult to predict in advance where HST will be in its orbit at a given time. The position error may be as large as 30 km within two days of a determination of the position of the spacecraft in its orbit.

Launch Date/Time	1990-04-25 at 12:33:51 UTC
On-orbit dry mass	11600.00 kg
Nominal Power Output	5000 W (BOL)
Batteries	Six – 60 Amp-hour NiMH
Orbital Period	96.66 m
Inclination	28.48 degrees
Eccentricity	0.00172
Periapsis	586.47 km
Apoapsis	610.44 km
Telemetry rates	0.500 - 1000.000 kbps
Effective Telemetry Rate	4.238 kbps

Figure 3.24 From STS82 - the second service mission - February 19, 1997
New solar arrays have not been deployed, yet. (S82E5937, 07:06:57)

2 The Hubble Telescope

The Hubble is an f/24 Ritchey-Chretien Cassegrain system with a 2.4 meter (94.5”) diameter primary mirror, and a 0.3 m secondary mirror. The primary mirror is constructed of ultra-low expansion silica glass and coated with a thin layer of pure aluminum to reflect visible light. A thinner layer of magnesium fluoride is layered over the aluminum to prevent oxidation and to reflect ultraviolet light. The secondary mirror is constructed from Zerodur, a very-low thermal expansion (optical) ceramic material. The effective focal length is 57.6 m.

The distance between the two mirrors is 4.6 m, the focal plane is 1.5 m from the front of the primary mirror. The angular resolution at 500 nm is 0.043 arc-seconds. Note that the corresponding requirement for the spacecraft was a pointing accuracy (jitter) of 0.007 arc-seconds. This was more easily achieved after the first set of solar arrays were replaced.

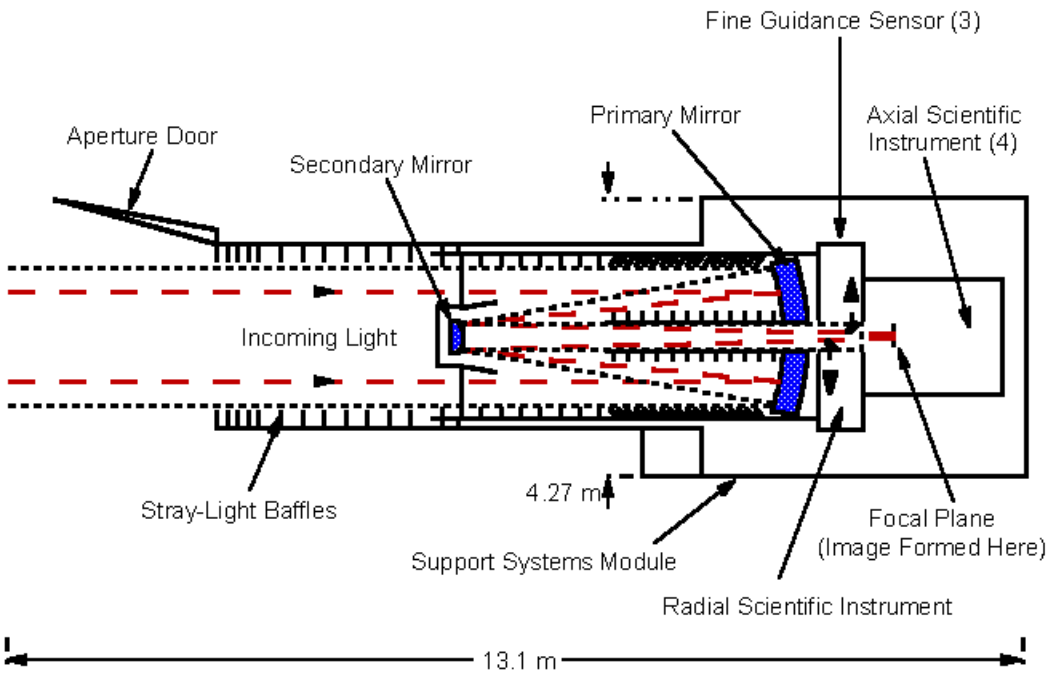

Figure 3.25 The Hubble Optics

There was just one small problem – the mirror was not ground to quite the right prescription, and it suffered from spherical aberration. As a consequence, new optics designs were created, and a very expensive corrective optic was applied for the existing instruments. Subsequent science instruments, such as the WFPC2, built corrections into their own optics.

Figure 3.26 The primary mirror of the Hubble telescope measures 2.4 m (8 ft) in diameter and weighs about 826 kg (1820 lbs). The center hole in the primary mirror has a diameter of 0.6 m.

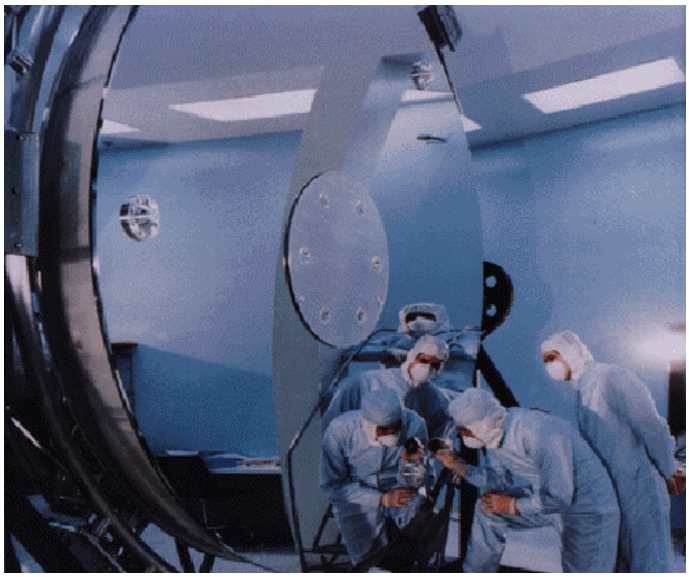

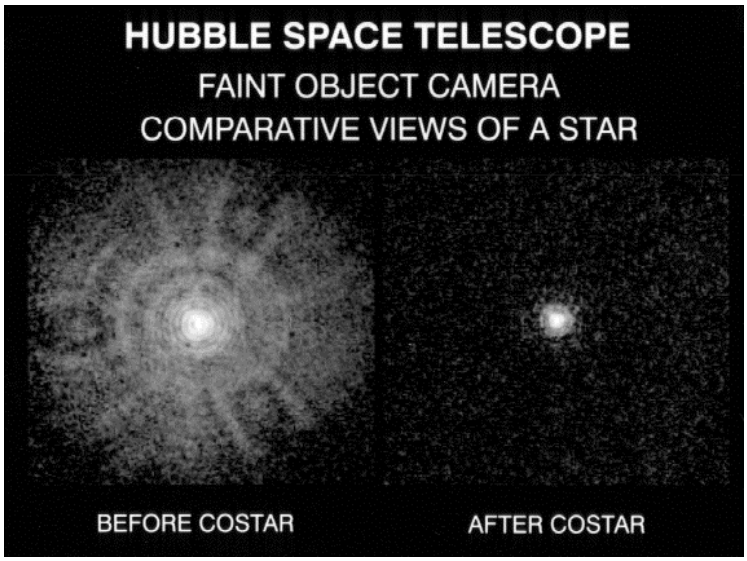

Figure 3.27: Left: An FOC image of a star taken prior to the STS-61 Space Shuttle mission to service the HST during which astronauts installed COSTAR. Right: Following the installation, deployment, and alignment of COSTAR, the starlight is concentrated into a 0.1 arc second radius circle.

3 Detectors - Wide Field Planetary Camera - 2

The Hubble normally carries 4 or 5 distinct sensors. For illustration purposes, the Wide Field and Planetary Camera 2 (WFPC2) is described here. *HST*'s Scientific Instruments are mounted in bays behind the primary mirror. The Wide Field Planetary Camera 2 occupies one of the radial bays, with an attached 45 degree pickoff mirror that allows it to receive the on-axis beam.

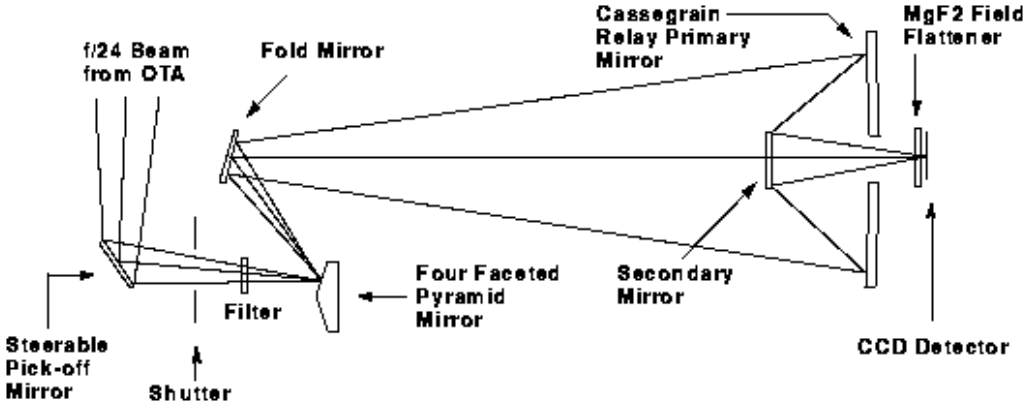

Figure 3.28 WFPC2 optics. Light enters the optical train from the main telescope at the left of the diagram.

The WFPC2 field-of-view is distributed over four cameras by a four-faceted pyramid mirror near the HST focal plane. Each of the cameras contains an 800 × 800 pixel Loral CCD detector. Three cameras operate at an image scale of 0.1" per pixel (F/12.9) and comprise the Wide Field Camera (WFC). The three cover an "L" shaped field-of-view of 150" x 150". The fourth camera operates at 0.046" per pixel (F/28.3) and is referred to as the Planetary Camera (PC). The fourth camera observes a smaller sky quadrant – a 34" x 34" square field. (Note that 34" is 34 arc-seconds, not 34 inches.) The spectral range lies from approximately 1150Å to 10500Å.

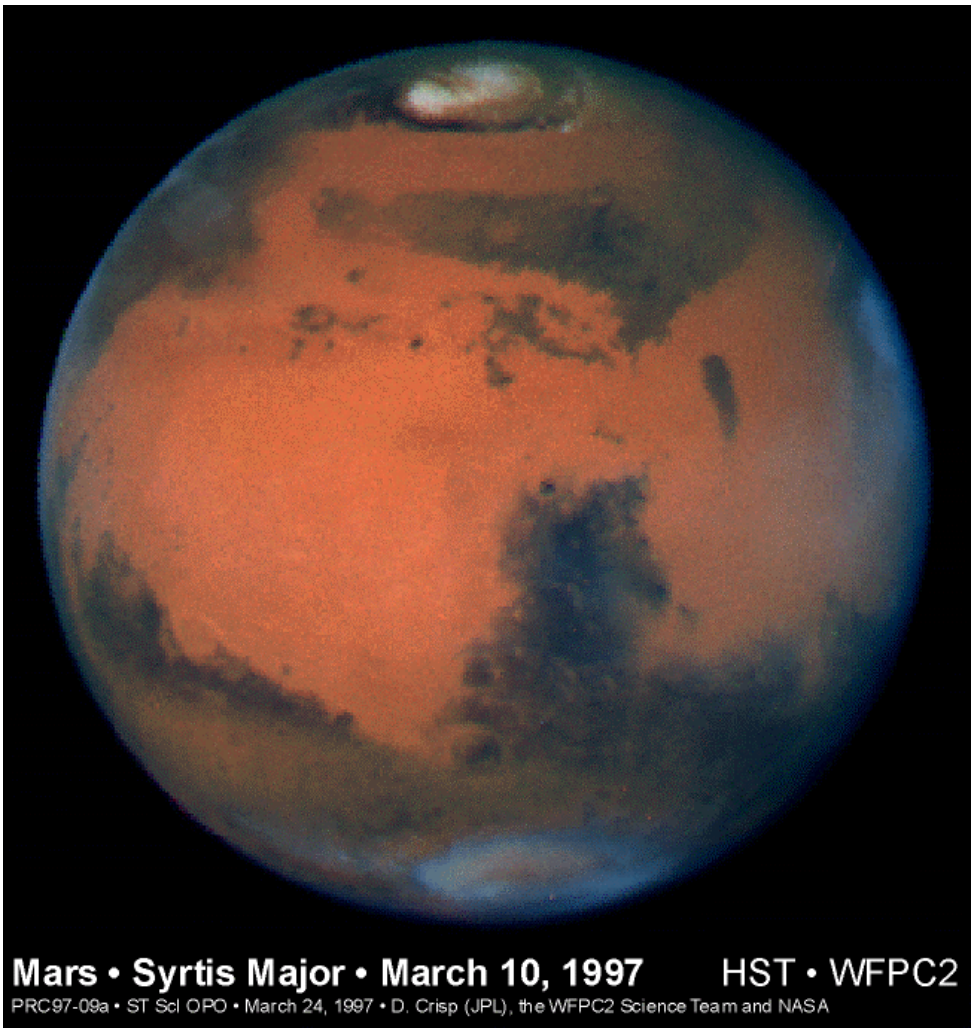

Figure 3.29 The sharpest view of Mars ever taken from Earth was obtained by the NASA Hubble Space Telescope (HST). This stunning portrait was taken with the HST Wide Field Planetary Camera-2 (WFPC2) on March 10, 1997, just before Mars opposition, when the red planet made one of its closest passes to the Earth (about 60 million miles or 100 million km). At this distance, a single picture element (pixel) in WFPC2's Planetary Camera spans 13 miles (22 km) on the Martian surface. The image is less than 335 pixels across - the Martian diameter is 6,794 km.

The WFPC2 was used to observe Mars in nine different colors spanning the ultraviolet to the near infrared. The specific colors were chosen to clearly discriminate between airborne dust, ice clouds, and prominent Martian surface features. This picture was created by combining images taken in blue (433 nm), green (554 nm), and red (763 nm) colored filters.

STScI-PRC97-09, March 20, 1997, David Crisp (JPL) and the WFPC2 Science Team

a Example: Diffraction and resolution limits

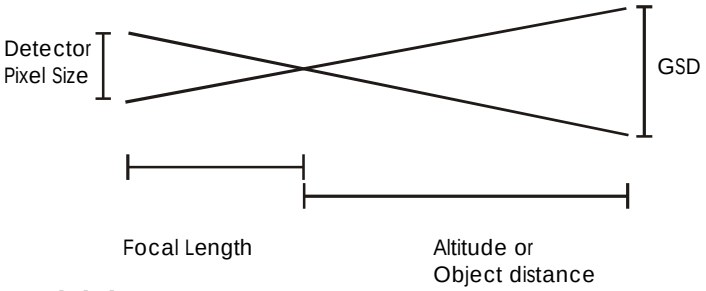

Figure 3.30 For the Hubble/WFPC2 combination, altitude is 600 km, detector size is 15 μ (microns), the focal length is 57 meters.

Rayleigh:

The angular resolution for the telescope is given as 0.043" (arc-seconds), with the slightly larger value of 0.046" for the combined Hubble/WFPC2 system. These values include all the effects which are ignored in the simplest approximation to the Rayleigh criteria,

$\Delta q = \dfrac{l}{lens\ (mirror)\ diameter}$. A few numbers are tested here.

$$\Delta q = \frac{0.043 \text{ arc-seconds}}{60 \text{ sec}/\text{min}\ 60 \text{ min}/\text{degree}} \bullet \frac{2p \text{ radians}}{360 \text{ degres}} = 2.08\times10^{-7} \text{ radians}$$

comparing, we get $\Delta q = \dfrac{5000\times10^{-10} \text{ m}}{2.4 \text{ m}} = 2.08\times10^{-7}$

Applying to the hypothetical problem of the ground resolution Hubble would have if pointed down, we get: $GSD = \Delta q \bullet \text{altitude} = 2.08\times10^{-7} \bullet 600\times10^{3} \text{ (meters)} = 0.125 \text{ m}$

If Hubble was pointed downwards, you would get a GSD of 12 cm. The calculations can be repeated for 0.046 arc-seconds, but the increase is only a few percent.

Resolution:

The above implies that the detector has infinite resolution. It does not, however. Using the concept of similar triangles shown previously, and the values for the detector pixel size given above, we can compare the detector resolution to the best resolution offered by the telescope.

$\dfrac{GSD}{altitude} = \dfrac{Pixel\ Size}{Focal\ Length}$; or

$$GSD = \frac{Pixel\ Size}{Focal\ Length} \bullet altitude = \frac{15\times10^{-6}}{57} \bullet 600\times10^{3} = 0.16 \text{ m}$$

which is slightly worse than the best the telescope can do – the Airy disk from a distant star, or small bright light on the ground, would not quite fill one detector pixel. The detector is "undersampling" the image.

I IKONOS

The world of remote sensing changed in a dramatic way in late 1999, when the first commercial high spatial resolution imaging satellite, IKONOS, was launched. Imagery which was previously the domain of "spy" satellites was now available to any customer.

1 THE SATELLITE:

IKONOS was built by Lockheed Martin Commercial Space Systems in Sunnyvale, California for Space Imaging. Designed to take images of the earth from 400 miles up in space, and moving at a speed of 4.5 miles per second, the satellite can collect imagery that will distinguish objects on the earth's surface as small as 1-meter square. The IKONOS satellite also carries a 4-meter resolution multi-spectral sensor.

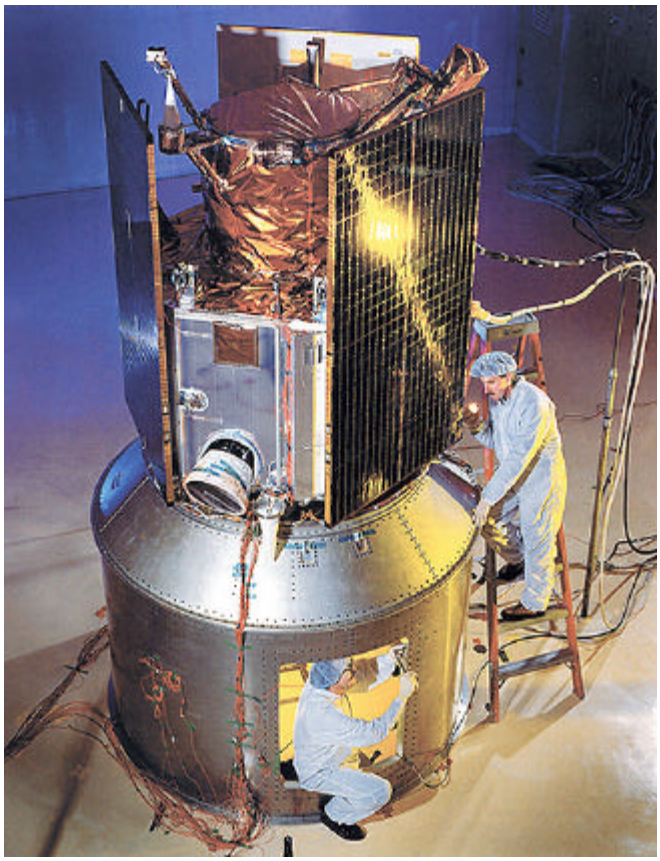

Figure 3.30. Image of the IKONOS satellite in the acoustic test cell at Lockheed Martin Missile & Space in Sunnyvale, CA. The satellite weight on the ground was less than 1,600 pounds.

Launch Information	Vehicle: **Lockheed Martin Athena II** Rocket Location: **Vandenberg Air Force Base, California**
Resolution	• Ground resolution of each band: **1-meter panchromatic (nominal at <26° off nadir)** **4-meter multispectral**
Revisit frequency	**2.9 days at 1-meter resolution;** **1.5 days at 1.5-meter resolution.** These values are for targets at 40° latitude. The revisit times will be more frequent for higher latitudes and less frequent for latitudes closer to the equator
Spectral Bands	Panchromatic: **0.45 - 0.90** m Multispectral: (same as Landsat TM Bands 1-4) **1: Blue 0.45 - 0.52** m **2: Green 0.52 - 0.60** m **3: Red 0.63 - 0.69** m **4: Near IR 0.76 - 0.90** m
Swath Widths & Scene Sizes	Nominal swath width: **• 11 km at nadir** Areas of interest: **• a single image at 11 km x 11 km** **• strips of 11 km x 100 km up to 11 km x 1000 km** **• image mosaics of up to 12,000 sq. km** **• up to two 10,000 square kilometer areas in a single pass within a region**
Metric Accuracy	**•12-meter horizontal and 10-meter vertical accuracy with no control** **• 2-meter horizontal and 3-meter vertical accuracy with GCP control** These are specified as 90% CE (circular error) for the horizontal and 90% LE (linear error) for the vertical
Orbital Information	Altitude: **681 kilometers / 423 miles** Inclination angle: **98.1**° Speed: **4 miles per second / 7 kilometers per second** Descending nodal crossing time: **10-11 a.m.** Revisit frequency**:** **3 days at 1-meter resolution;** **1.5 days at 1.5 meter resolution** Orbit time: **98 minutes** Orbit type: **sun-synchronous** Viewing angle: **Agile spacecraft - in-track and cross-track pointing** Weight: **1600 pounds**

2 Imaging Sensors and Electronics for the IKONOS Satellite

a The Camera System

The Kodak digital camera system for IKONOS consists of four major elements:

- The Optical Telescope Assembly captures the imagery across an 11-km to 13-km swath of the Earth's surface, and reflects it to the digital imaging sensors.
- The Focal Plane Unit contains panchromatic (black and white) and multispectral (color) imaging sensor arrays that transform the light into distinct picture elements (pixels). An analog signal processor converts the light striking each pixel into digital bits.
- The Digital Processing Unit compresses and formats the digital imagery for transmission to ground.
- The Power Supply Unit regulates power from the spacecraft to the camera electronics.

b Camera Telescope

Telescope design: The camera telescope has the equivalent resolving power of a 10,000mm telephoto lens. Three of the five telescope mirrors are curved, and are used focus the imagery onto the imaging sensors at the focal plane. Two flat mirrors, known as fold mirrors, bounce the imagery across the width of the telescope, thereby reducing overall telescope length from 10 meters to about two meters.

Weight reduction: To reduce overall telescope weight, Kodak cut out a significant portion of the glass from the telescope's largest (primary) mirror. The honeycomb glass core that remained was covered with thin, front surface mirror top and bottom glass faceplates, which were polished.
Surface polishing: To ensure the sharpest imagery possible, the surfaces of the three curved mirrors were polished to atomic level accuracy. The primary mirror surface is so smooth, if it were enlarged to 100 miles (160 km) in diameter, a car driven across its surface would not hit bumps any higher than 0.08in, or 2mm.

Mirror alignment: Two of the optics can be adjusted for focusing by command from the ground should correction be necessary. Mirror alignment, together with surface polishing accuracy, enable the telescope to deliver the sharpest possible image to the imaging sensors at the focal plane.

c Imaging Sensors & Electronics

Sensor arrays: The camera's Focal Plane Unit - attached to the back end of the telescope - contains separate sensor arrays for simultaneous capture of panchromatic (black and white) and multispectral (color) imagery.

The panchromatic sensor array consists of thousands of 12-micron-sized pixels (picture elements) . To capture red, green, blue and near-infrared light, the multispectral array is coated with special filters.

Digitizing the light: The CCD sensor arrays convert the light striking each pixel into discrete electronic charges. These charges are then measured as digital values by an analog signal processor in the Focal Plane Unit.

Image compression: The Digital Processing Unit compresses the digital image files from 11 bits per pixel data to an average value of 2.6 bpp at a speed of 115 million pixels per second.

Power: The Power Supply Unit converts electrical power from the spacecraft for use by the camera subsystems. Total camera system energy consumption is equivalent to a desktop PC.

d Quick Facts

Camera System

Total system weight: 376 lbs. (171 kg.)
Total system power consumption: 350 watts

Optical Telescope Assembly

Assembly size: 61in. long x 31in. wide (1524mm) x (787mm)
Assembly weight w/out focal plane unit: 240 lbs. (109 kg.)
Optical design: Three mirror anastigmat
Focal length / focal ratio: 10m / f14.3
Image resolution (at nadir): one-meter panchromatic, four-meter multispectral
Primary mirror: 27.5in. (0.7m) diameter x 4in. (100mm) thick, 29.5 lbs. (13.4 kg.)

Imaging Sensors & Electronics

Focal Plane Unit

Unit size: 10in. x 9in. x 9in. (25cm x 23cm x 23cm)
Panchromatic sensor: 12 micron pixel pitch, 13,500 pixels
Multispectral sensor: 48 micron pixel pitch, 3375 pixels

Digital Processing Unit

Unit size: 18in. x 7.5in. x 12.4in. (46cm x 19cm x 31cm)
Compression rate: 11 bits per pixel compressed to 2.6 bpp
Compression speed: 4 million pixels per second per processing channel

Power Supply Unit

Unit size: 7in. x 8in. x 16in. (18cm x 20cm x 41cm)

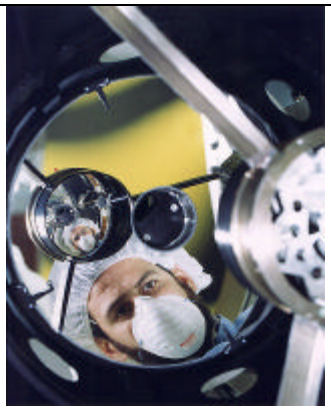

Figure 3.31.a IKONOS Camera:
A Kodak technician is reflected in the largest of three curved mirrors inside the compact IKONOS telescope assembly.

Figure 3.31.b
IKONOS Camera: Focal Plane array. A Kodak technician exposes the focal plane array at the base of the telescope

Figure 3.32 IKONOS Camera: Telescope

The IKONOS telescope has the equivalent resolving power of a 10,000mm telephoto lens. Designed and built by Kodak, the telescope features three curved mirrors, each precisely figured to capture and focus high-resolution Earth imagery onto the imaging sensors at the focal plane. Two additional flat mirrors 'fold' the imagery across the inside of the telescope, thereby significantly reducing telescope length and weight.

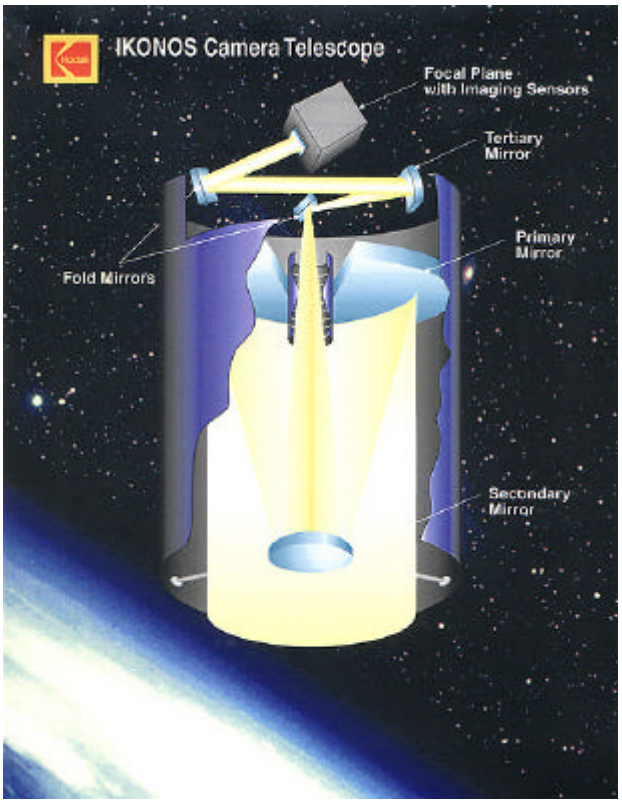

.
http://216.33.193.141/events/spaceimaging/aboutkodak2.html

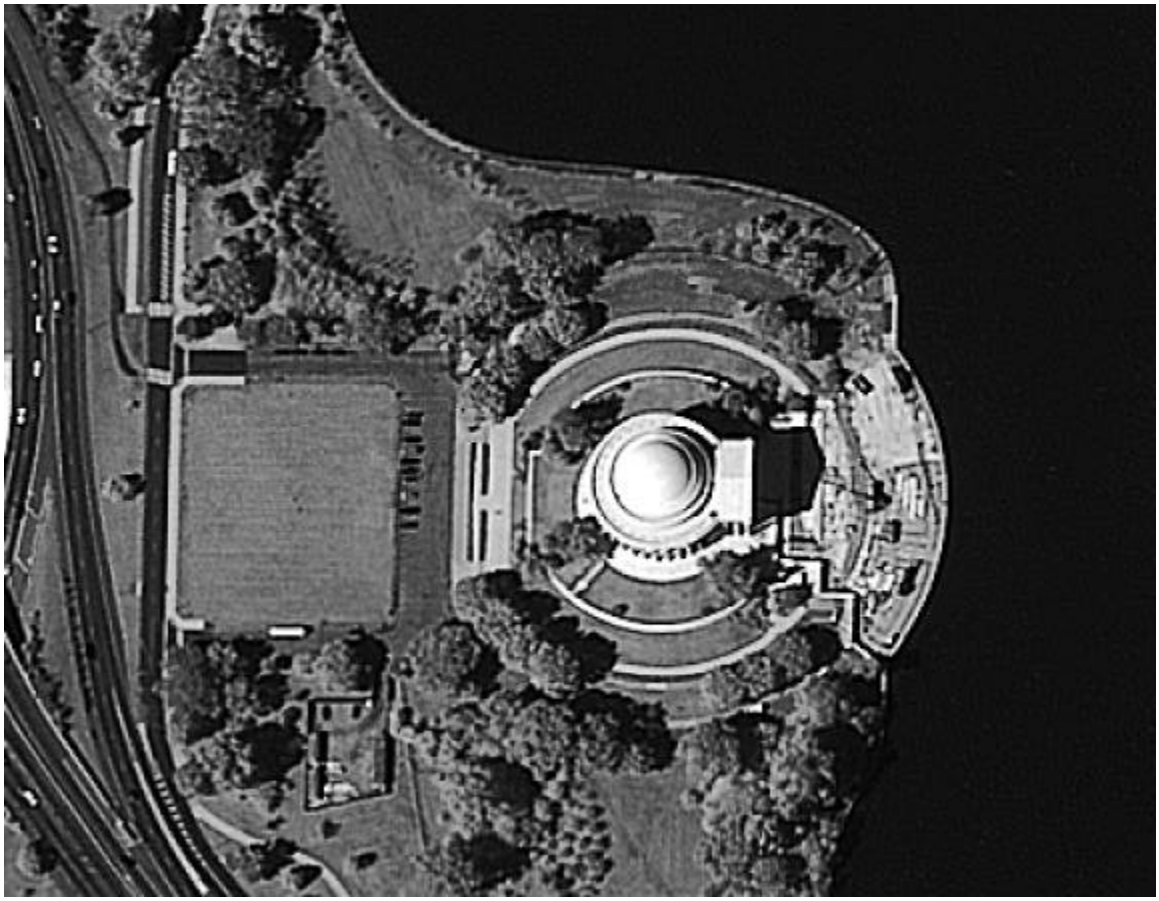

Figure 3.33 Washington DC - part of the first IKONOS image.

J DMSP - visible sensor - earth at night

Defense Meteorological Satellite Program (DMSP) satellites are primarily intended to gather weather data for military purposes. The system is presented here as an illustration of the concept of low-light level imaging. This system consists of platforms in sun-synchronous orbits with dayside equatorial crossings at 6:00 AM and 10:30 AM local times. Their purpose is to assist forecasters to identify and track developing patterns of weather so that imaging reconnaissance satellites do not waste film and flying time. Characteristics of some of the most recent 'Block 5D-2' missions are given here.

Common Name	DMSP 5D-2-F11	DMSP 5D-2-F12	DMSP 5D-2-F13	DMSP 5D-2-F14
International Number	1991-082A	1994-057A	1995-015A	1997-012A
Launch Date (YYYY/MM/DD)	1991/11/28	1994/08/29	1995/03/24	1997/04/04
Launch Time	1323	1738	1405	1647
Mass	830.0 kg	823.0 kg	823.0 kg	850.0 kg
Apogee	853 km	858 km	855 km	855 km
Perigee	836 km	839 km	843 km	841 km
Period	101.8 min	101.9 min	101.9 min	101.8 min
Inclination	98.9°	98.7°	98.9°	98.8°

These satellites measure roughly 1.22m $\times$ 6.4m, with one solar wing of 8 panels generating one kW.

The OLS instrument consists of two telescopes and a photo multiplier tube (PMT). The scanning telescope of the OLS has a 20-cm aperture with an effective collecting area of 239 cm^2 and effective focal length of 122 cm. Light is split into two channels by a beam splitter. The system is designed to produce constant high resolution imaging rather than accurate radiometry.

The detectors sweep back and forth in a "whisk broom" or pendulum-type motion. The continuous analog signal is sampled at a constant rate so the Earth-located centers of each pixel are roughly equidistant, i.e., 0.5 km apart. 7,325 pixels are digitized across the 108° (???) swath from limb to limb.

Telescope pixel values are replaced by Photo Multiplier Tube (PMT) values at night. A telescope pixel is 0.55 km at high resolution (fine mode) and 2.7 km at low resolution (smooth mode). Low-resolution values are the mean of the appropriate 25 high resolution values. A PMT pixel is 2.7 km at nadir. Visible pixels are currently relative values ranging from 0 to 63 rather than absolute values in Watts/m^2. Instrumental gain levels are adjusted to maintain constant cloud reference values under varying conditions of solar and lunar illumination. Note that the combination of the two visible detectors allows a dynamic range of 2^5.

Swath (Scan Angle): 3000km @ 833km altitude

Spectral Channels	Wavelength (μm)	Wavelength (FWHM, μm)	Sensitivity	Spatial Resolution
OLS-L	0.40 - 1.10	0.58 - 0.91	10^{-3} - 10^{-5} Watts/cm^2 per sterradian	0.56 km*
OLS-PMT	0.47 - 0.95	0.51 - 0.86	10^{-5} - 10^{-9} Watts/cm^2 per sterradian	2.7 km
OLS-T	10. 0 - 13.4	10.3 - 12.9	190 to 310 K	5.4km

* stored data are resampled to 2.7km;

Figure 3.34 Several months of data, with cloudy data removed. The image is resampled to 1 km resolution.

.

K Problems

1. When was the first Corona launch ?

2. When was the first successful launch? Which number was it?

3. How many launches before they had a successful film return?

4. How did the date of this launch compare to that of the U-2 incident with Gary Powers?

5. What was the best resolution (GSD) of the KH-4 cameras reported upon in this document?

6. What was the swath width associated with the 'best' resolution KH-4 images?

7. How many CORONA missions were there?

8. List 5 elements of recognition.

9. How could you tell that a road or rail-line was intended for missile transport.

10. When is the best time of week(day) to inventory an opponent's hardware (seems like it depends on religion...)

11. What is the focal length, diameter, and f/# for the Hubble Primary Optic?

12. Locate a high-quality 200 mm lens for a good 35 mm camera (say a Nikon or Canon). What is the f/#? What diameter is the primary optic?

13. For a 24" focal length camera, f/3.5, at an altitude of 200 km, calculate the GSD corresponding to a 0.01 mm spot on the film. Assume nadir viewing. Note that this is a geometry problem.

14. For a 24" focal length, f/3.5 lens, calculate the Rayleigh limit to GSD for a satellite at 200 km altitude. Assume nadir viewing, visible light (500 nm).

15. What diameter mirror would be needed to achieve 12 cm resolution (GSD) at geosynchronous orbit (6.6 Re, geocentric - note that this is **not** the altitude).

16. What are the three factors which constrain the resolution which can be obtained with an imaging system?

17. Adaptive optics: compare the Rayleigh criteria for the 3.5 m starfire observations in figure 3.17 to the results with and without the adaptive optics

18. Adaptive optics:

<table>
<tr>
<td> 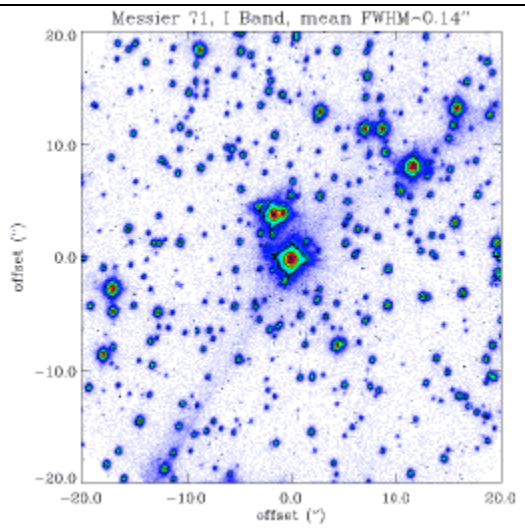
</td>
<td> 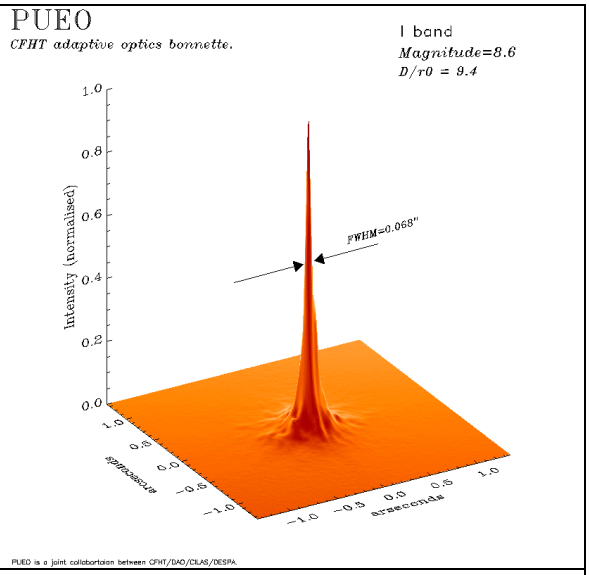
</td>
</tr>
<tr>
<td>This is an image of the center of the globular cluster M71 at I band (830 nm). FWHM is 0.10 arcsec (center) to 0.18 arcsec (edges). The natural seeing was 0.30 arcsec (excluding tracking errors and telescope fixed aberrations). This is a 1200 seconds exposure.</td>
<td>Image of an 8.6 R magnitude star in the I band. The FWHM is 0.068 arcsec. "To our knowledge, this is the crispiest long exposure image ever from ground based observations. " 2 second exporsure.</td>
</tr>
<tr>
<td colspan="2">http://www.cfht.hawaii.edu/Instruments/Imaging/AOB/mai_run.html
May 3-8, 1996, Canada-France-Hawaii Telescope (CFHT) adaptive optics compensation system. Also called PUEO after the sharp vision Hawaiian owl. The telescope is 3.6 meter in diameter. The observatory is located atop the summit of Mauna Kea, a 4200 meter, dormant volcano located on the island of Hawaii.</td>
</tr>
</table>

Compare the observed FWHM of 0.10 arcsec to the Rayleigh limit for such a mirror. Repeat for the "natural seeing" conditions of 0.3 arcsec.